

Overview of a planned flight test operation for a scaled in-air capturing demonstration

Stefan Krause, Sebastian Cain*, and Alexander Funke**

**DLR (German Aerospace Center), Institute of Flight Systems, Department of Unmanned Aircraft
Lilienthalplatz 7, 38108 Braunschweig, Germany, stefan.krause@dlr.de*

*Joaquín González** and Mario Ferrándiz***

***Embention*

PI. Atalayas, C/ del Chelín, 16, 03114 Alicante, Spain, joaquin.gonzalez@embention.com

Abstract

Current aerospace research seeks to realize reusable launch vehicle (RLV) missions. One conceptual idea is to capture a returning booster stage in air with another aircraft as proposed by DLR in previous work. Within the H2020 project - **Formation flight for in-Air Launcher 1st stage Capturing demonstration (FALCon)**, we investigate the in-air-capturing (IAC) approach with a demonstration setup of scaled unmanned aerial vehicles to research different aspects of this approach in scaled flight tests.

This paper provides an overview of the unmanned IAC demonstrators and the planned experiment setup of the FALCon project, which will be validated in future flight test demonstrations. We describe the details of three flight demonstrators for the reusable launch vehicle, capturing or towing aircraft, and an intelligent coupling device which we developed from scratch for this project. We focus on the safety aspects enabling the implementation of a safe and successful demonstration in a non-segregated European airspace and present our researched aspects of the IAC maneuver. The planned formation requires a relative pose estimation between the involved demonstrators, while the demonstrators perform a rapid unpowered descent. We use an environmental perception setup, based on camera and LiDAR data processing, to solve this challenging task.

1. Introduction

The reduction of costs is the main motivation for reusable booster stages or complete spaceships for several missions [1], [2]. The key challenge to enable reusability is to develop a safe and nondestructive retrieval of the stage from high altitudes to a specified landing position. There are several ways to approach such retrieval. One is to use the booster's own propulsion and fuel reserves as demonstrated by SpaceX [1]. Another approach, which we pursue in our work, is to capture the returning stage, the Reusable Launch Vehicle (RLV), while airborne with an aircraft which tows it to the landing destination [3]. This method is called In Air Capturing (IAC) and Figure 1 shows a concept sketch of the capturing maneuver for a winged booster stage [4]. The IAC's main advantage is the reduction of mission fuel which allows to increase mission payload when compared to a retrieval with fuel reserves using the booster's own propulsion. However, the applicability of this method still needs to be successfully demonstrated.

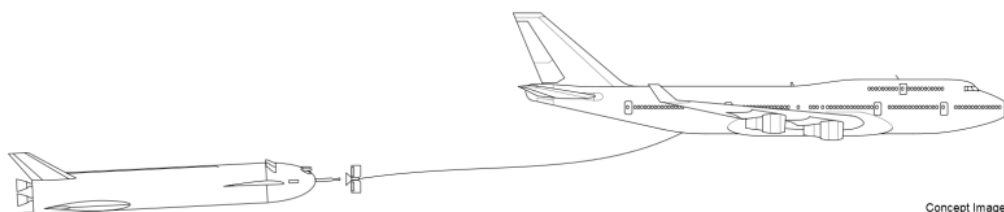


Figure 1: Concept for the IAC method with LFBB and Boeing 747

We assume, that the RLV has only limited controllability and no propulsion after reentry from orbit and thus has the flight performance of a passive glider with poor flight characteristics and high inertia. A possible towing aircraft could be a modified civil or military transport aircraft, which has the necessary excess power for towing the booster stage. However, the high mass and limited maneuverability of the vehicles increases the difficulty of the IAC maneuver.

Air-to-air refueling (A2AR) maneuvers with the probe-drogue method [5] is like IAC regarding the reversible coupling of two aircraft while in flight, and thus serves as an example for the proposed IAC task. For the A2AR procedure, a fighter aircraft, usually an aircraft with high maneuverability which is equipped with a probe, approaches a less agile tanker aircraft that tows the drogue. The more agile fighter performs the approach while tracking the drogue and compensating for any disturbances. The tanker aircraft maintains steady flight during the maneuver. The same principle can be used for the IAC maneuver but with the additional challenge of establishing contact between RLV and towing aircraft, which both have limited maneuverability and agility. Compensation of disturbances leading to deviations of the relative position less effective if performed by the by the towing aircraft is, because corrections of the towing aircraft do not affect the position of the drogue instantaneously. Instead, the flexible connection between towing aircraft and drogue results in significant delays for corrections to take effect.

To overcome the delays and limited maneuverability of both vehicles, we proposed an actuated drogue that can adjust its relative position. The drogue is equipped with an avionic system and changes its position by either changing the length of the cable for longitudinal motion or controlling its lateral and vertical position with aerodynamic control surfaces [6], [7]. This controlled drogue is referred to as an Aerodynamically Controlled Capturing Device (ACCD). The in-flight capturing maneuver poses high-risks of collision between the vehicles. Thus, we seek to fully automate the returning booster stage and to use an unmanned towing aircraft, which must be automated as well. To allow for active positioning of the ACCD with respect to the booster, it is necessary to estimate the relative position between them. The position estimation can be based on GNSS data or image sensors and is used to calculate the offset, which is compensated by the ACCD flight control system. Due to the limited accuracy of GNSS information, the resulting offsets are only suitable for a rough positioning of the vehicles in a first step. A more accurate method, such as image processing, can be used afterwards to control the ACCD's position more precisely.

The concept on IAC-maneuver is an early state and contains some open questions. To detail the concept, the EU funded the project “Formation flight for in-Air Launcher 1st stage Capturing demonstration” (FALCon) [8] [9] for the purpose of investigating some of these questions with conceptional studies, simulations, and scaled flight tests. The purpose of this paper is to present an overview about the scaled flight test operations which are part of the FALCon project. Especially, we focus on the technology demonstrators used for flight testing, the optical based environment perception, and the mission design as well as its implementation.

The subsequent Section 2 gives an overview of the project's scaled experiment demonstration with fundamental descriptions of the IAC phase, the requirements adopted from the real scenario, the planned mission, and the mission's implementation into an experiment. Section 3 contains a description of the three involved technology demonstrators. In Section 4, we present the environment perception setup that we intent to use for our demonstration to get a position feedback of the ACCD in relation to the RLV. We share the results of recently completed simulation experiments of the environment perception algorithms. Finally, we conclude the paper with a summary and an outlook on future work.

2. Scaled Experiment Scenario Demonstration

The IAC maneuver is part of the RLV-circle which was presented in previous publications, i.e., [7]. The aim of the scaled demonstration in the FALCon project is to demonstrate the IAC phase, without the surrounding phases.

The IAC phase, as it is meant in the FALCon project, contains two sub phases:

1. **Rough Formation:** A formation flight between the Winged Reusable Launcher Vehicle Demonstrator (RLVD) and the Towing-Aircraft Demonstrator (TAD). During this sub phase, the RLVD publishes its state and the TAD tries to achieve a formation position straight in front of the RLVD. After the TAD arrives its target relative position, it maintains a steady flight condition for whole IAC maneuver.
2. **Fine Formation:** The TAD holds a steady relative position to the RLVD while the ACCD automatically controls its position to establish a connection to its counterpart at the RLVD nose. The ACCD motion is monitored by vision-based perception which delivers a position feedback to the ACCD controller about the deviation between the both connection points.

The consideration of the IAC maneuver in the FALCon project ends with the contact between ACCD and RLVD. A physical locking or a towing of the RLVD by the TAD is not intended to avoid the safety threat to both demonstrator vehicles that is introduced by the fixed connection. Also, the size and the limited power of the applied Unmanned Aircraft Vehicles (UAVs) prevent a towing.

During the IAC-maneuver, the non-propulsive RLVD follows a straight path with -10° descent angle. These requirements base on the real scaled concept and they are considered to enable the transferability of the results. The maneuver will be implemented in altitudes between approx. 655 m and 100m above ground level. The altitude boundaries base on legal requirements set by the test facility which result from its local air space structure and the its close proximity to inhabited areas. An overview of the mission path is shown by Figure 2. The entry point E marks the entry of the experimental path of the RLVD demonstrator. The separation point S marks the end of the IAC maneuver, the separation of the formation, and the start of the independently conducted landing of the single aircraft. The velocity

of the RLVD between E and S is designed to be ca. 42 m/s (150 km/h). Based on this parameter, the flight path covers a downrange distance of approx. 3100 m and a flight time of 73 s.

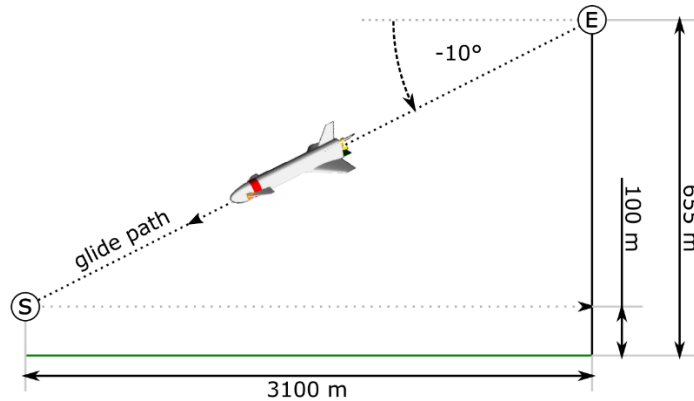


Figure 2: Overview of scaled scenario measuring section

Both subphases require an information exchange between the different vehicles. Figure 3 presents an overview of the communication connections as implemented in the scaled demonstration setup of the FALCon Project.

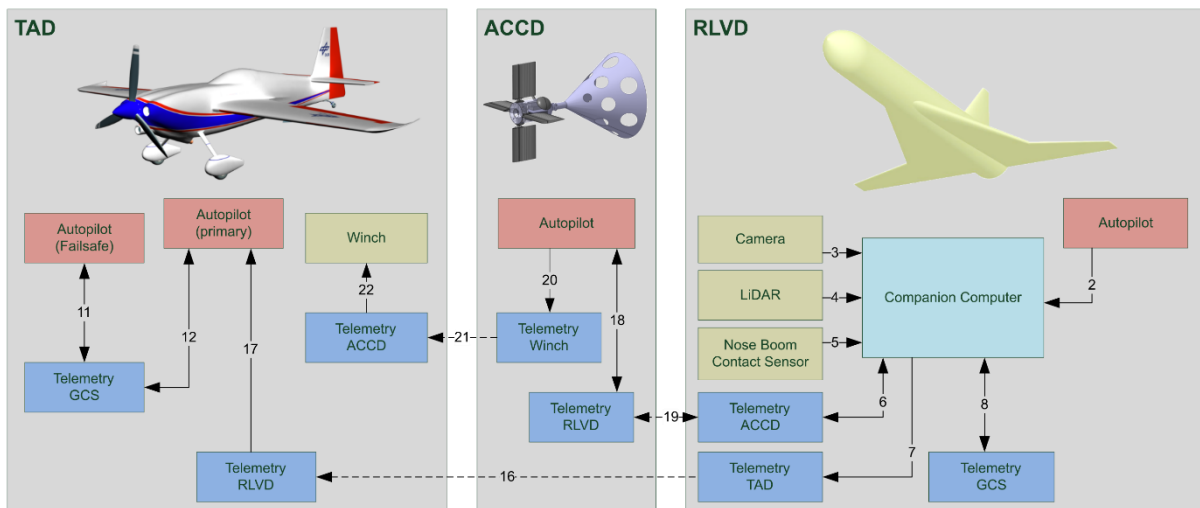


Figure 3: Datalink and communication overview of scaled FALCon demonstrator setup

Figure 3 shows the three demonstrators with their internal wiring for communication and three datalinks to communicate between the demonstrators. The components are divided in four classes: autopilots in red, datalinks in blue, payload or sensors in pastel green, and the companion computer of the RLVD as central processing unit in turquoise. See Section 3 for more detailed descriptions of the internal components of each vehicle and Section 4 for more information of perception sensors of the RLVD.

The datalinks 16, 19, and 21 shown in Figure 3 are relevant to exchange the required information during the IAC phase. The RLVD uses datalink 16 to publish its own state. The TAD uses this information to build up the rough formation. The state, published by the RLVD, contains its position and velocity. Datalink 19 is used for bidirectional data exchange between ACCD and RLVD. The ACCD publishes its estimated absolute position to the RLVD, where this information is used as input for the sensor data fusion of RLVD. The RLVD navigation software fuses GNSS sensors, inertial navigation sensors, air data sensors, and observations of the optical sensors in the nose of the RLVD to estimate its relative position to the ACCD. The relative position estimate is transmitted back to the ACCD via Datalink 19. See Section 4 for a detailed description of the optical sensor system. Datalink 21 carries control commands of the ACCD to the winch, mounted on the TAD, to adjust the longitudinal position of the ACCD by changing the cable length. All motions of the ACCD are computed by the ACCD autopilot, which either controls the aerodynamic control surfaces or determines the desired cable length as input to the winch controls.

The flight demonstrations and tests will be conducted at the National Experimental Test Center for Unmanned Aircraft Systems located in Cochstedt near Magdeburg in northern-central Germany. The test site is operated by the German Aerospace Center (DLR). The flight demonstrations and tests require the approval of the responsible German Federal

Aeronautic Authority (LBA) following the guidelines and requirements of the Specific Operations Risk Assessment (SORA) process implemented by the European Aviation Safety Agency (EASA). SORA defines a Specific Assurance and Integrity Level (SAIL) based on size, performance, and safety equipment of involved UAS platforms as well as mission complexity, and possible harm to uninvolved third parties. SORA requirements for our intended demonstrations and tests base on SAIL II.

The reduction of possible risks and compromise to third parties plays a major role in our preparation of documents for approval and the flight tests itself. Thus, we frequently must reconsider safety aspects and mitigation actions. The demonstration is planned with several procedures (e.g., emergency response plans) and safety margins that are documented in the operation handbook to cover possible malfunctions of the demonstrators or errors of the crew. A major task is the design safety buffers to avoid populated areas, to prevent a fly away of the demonstrators, and to reduce influences to third parties on ground and in the air to a minimum. Figure 4 gives an overview of the Cochstedt area, the planned operation geometry (green overlay), contingency area (yellow overlay), and ground risk buffer (red overlay). The points E and S are corresponding to the points in Figure 2. The contingency buffer has a dimension of 157 m, that bases on the operation velocity and the minimal turn radius of the demonstrator in combination with the reaction time of the crew or an automatic system to initiate a contingency operation. The red line indicates the route of a street which divides the test area into one part in the East and one part in the West of the street. The western part of the ground risk buffer has a maximal dimension of 1870 m. The eastern side of the buffer has a maximal dimension of 815 m. The dimension of the ground risk buffer is defined by the operation altitude over ground level (AGL), possible wind drifts, and the descent velocity in the case of a rescue parachute operation. The maximal operation height is 655 m AGL at the western part. On the eastern part, the height is 330 m AGL.

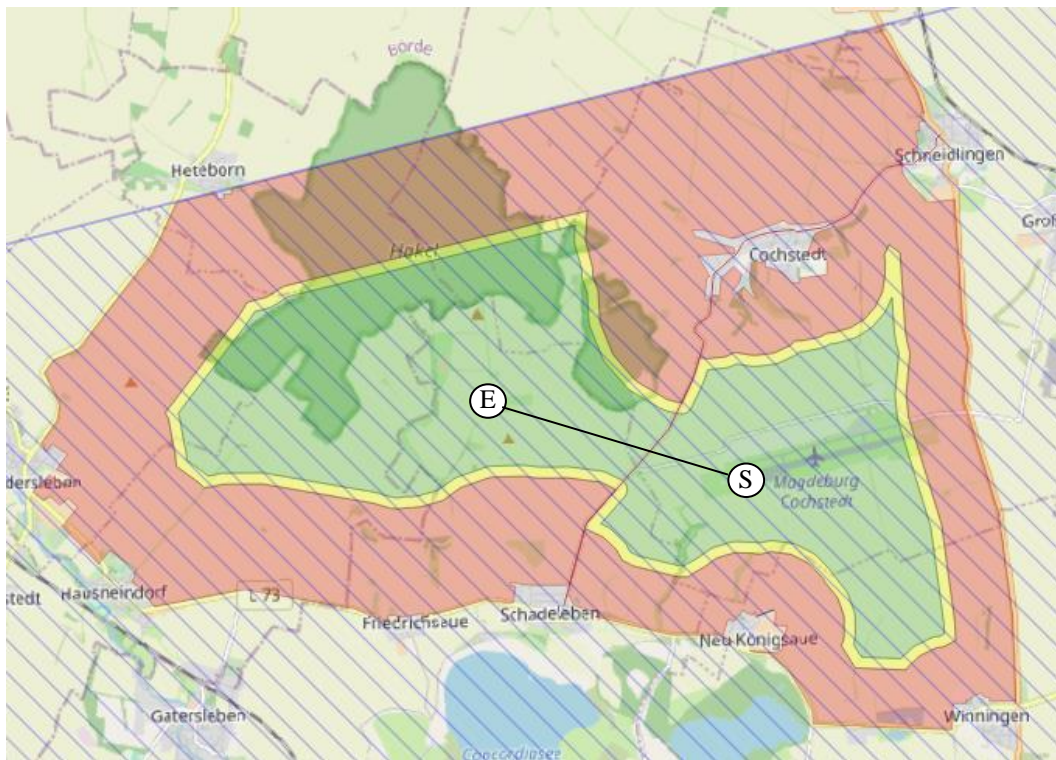
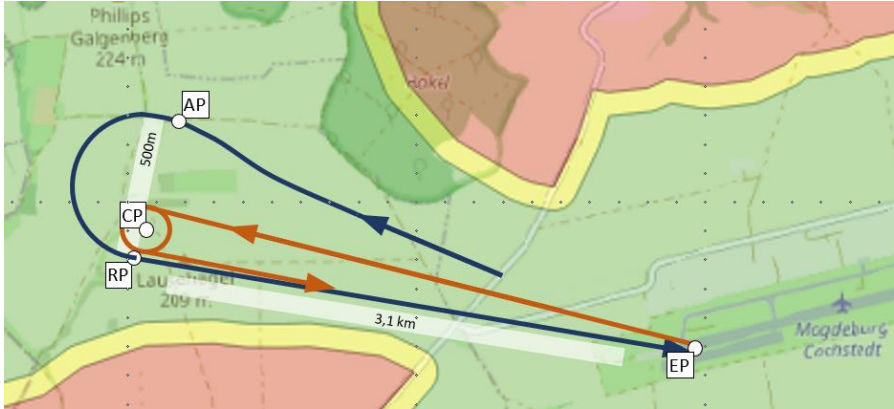


Figure 4: Mission area at Cochstedt, Germany, with mission track and operation volume (green), contingency buffer (yellow), and ground risk buffer (red)

Supplementary to the strategic mitigation actions like the risk and contingency buffers, we integrated special safety equipment into the demonstrators. We use an ADS-B in receiving mode only and FLARM to detect possible present manned air traffic on and around the test site to avoid in-air collision. We mitigate unrecoverable malfunctions of the demonstrators with rescue parachutes to reduce ground impact energy which reduces the possibility of lethal injuries to people on the ground. See Section 3 for a more detailed description of the demonstrators and their safety systems. The measurement track as presented in Figure 2 requires a preparation phase to achieve the initial conditions of the IAC maneuver. These conditions are defined by the RLVD, which performs an unpowered descent of -10° and approx. 150 km/h.

We divide the preparation phase into the starting phase and the rendezvous phase. These phases are complemented by the two subphases of the IAC-maneuver to a total of four phases, which need to be implemented. Figure 2 presents the top view of the whole operation track including the measurement track. The IAC measurement track is located between the reference point (RP) and the endpoint (ER), which corresponding to the entry point and separation point in Figure 2.



RP	Reference point
EP	Endpoint of mission
CP	Circle point, center of holding pattern for towing aircraft
AP	Adaptation point

Figure 5: Mission trajectory in flight area

As mentioned before, the IAC measurement track is only the central part of the experiment. The single phases to implement the IAC maneuver are present in the follow itemization according to Figure 5.

Starting phase: The TAD towing the ACCD takes off while being manually controlled by a pilot. After a system check, the control is handed over to the autopilot. Then, the TAD arrives at the circle point (CP) where it performs a circular shaped holding pattern. Subsequently, the RLVD takes off, and arrives at the adaption point (AP). The radius of the TAD holding circle is chosen so that the time to follow the whole equals the time for the RLVD to follow its semi-circular path from point AP to the reference point RP.

Rendezvous phase: In this phase, the TAD maintains its circular loitering maneuver while the RLVD is heading to the adaptation point AP and climbing to 655m AGL. After arriving at the AP, the RLVD starts to broadcast its position and while flying horizontally on a predefined semi-circle path to the reference point RP. Based on the published RLVD state, the TAD autopilot computes interception parameters (velocity and a new circle radius) to get in front of the RLVD when it arrives at RP.

Formation phase: Shortly before reaching RP, the RLVD changes to engine idle mode and initiates the -10° glide path angle. Based on the previous rendezvous phase, the TAD is near to the RLVD and starts to get ahead of the RLVD by adapting its glide path. The aim is to achieve a formation flight between both vehicles. We assume for the initial formation that the TAD is approx. 30 m ahead of the RLVD whereas the lateral deviation from the RLVD course is very small.

Capture phase: As the TAD arrives in the final formation position (procedure contains several sub steps), the ACCD starts to actively control its relative position. The perception, sensors and processing, carried by the RLVD detects the ACCD and publishes the position feedback to the ACCD. The aim of the ACCD controller is to its control surfaces and the winch of the TAD in order to reduce its deviation to the RLVD nose. RLVD and TAD maintain a steady flight condition to keep their formation positions while the ACCD is active. When the TAD arrives at the EP point, the ACCD is deactivated and the formation dissolves.

3. Flight Test Demonstrators

The following subsections presents the setups of the three demonstrators which we build up in the FALCon project to investigate the IAC maneuver. To distinguish between our scaled demonstrators and the real vehicles, we refer to our scaled demonstrators as demonstrators. One exception is the ACCD, which we designed specifically for our scaled demonstrations, and thus has no real scale counterpart.

3.1. Reusable Launch Vehicle Demonstrator

The Reusable Launch Vehicle Demonstrator (RLVD) is an unmanned experimental aircraft intended to simulate the aerodynamic behavior of a reusable winged launcher (e.g., Liquid Fly Back Booster or Space Liner studies of DLR) in the scaled experiment. The requirements that must be represented by the RLVD are: a L/D-ratio between 6 and 7, COG_x at approx. 70% length measured from the nose, and a delta wing configuration.

To achieve these requirements, the delta wing configuration shown by Figure 6 is used. This configuration bases in a Rapier Jet setup with rudders in the two winglets instead of one central rudder. The MTOW of the aircraft is 75 kg and it is powered by one jet engine with maximal thrust of 390 N, which is located in the central rear part of the fuselage. The landing gear is a fixed tricycle configuration which allows a horizontal takeoff and landing from a landing strip.

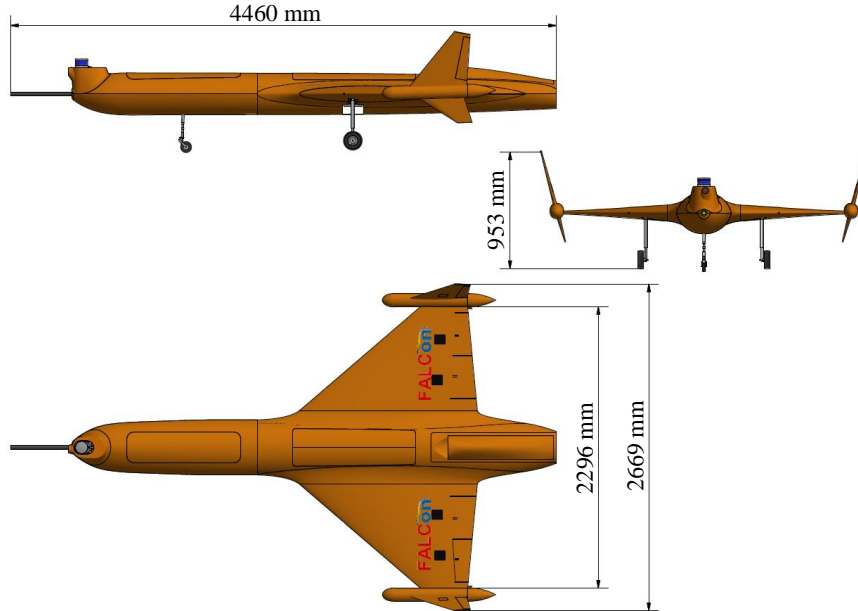


Figure 6: RLVD 3Side View

The RLVD combines six aerodynamic surfaces for three primary controls and one secondary control (see Figure 7). The three primary controls for pitch, roll, and yaw are implemented as follows. The pitch motion is controlled by an up and down motion in the same direction of all elevons and flaperons. The roll motion is controlled by moving elevon and flaperon on one side differentially to the ones on the other side. Yaw control makes use of both rudders, which move in the same direction. For the secondary control, the air speed brake, the elevon, and flaperon on each wing are differentially moved to each other. In this case, the flaperons move downward to reduce the stall speed and to increase the drag ratio while the elevons move upwards to compensate the pitch moment and to reduce the lift ratio. The RLVD is controlled by the 1X Veronte autopilot which uses a proprietary real-time software developed by Embention [10].

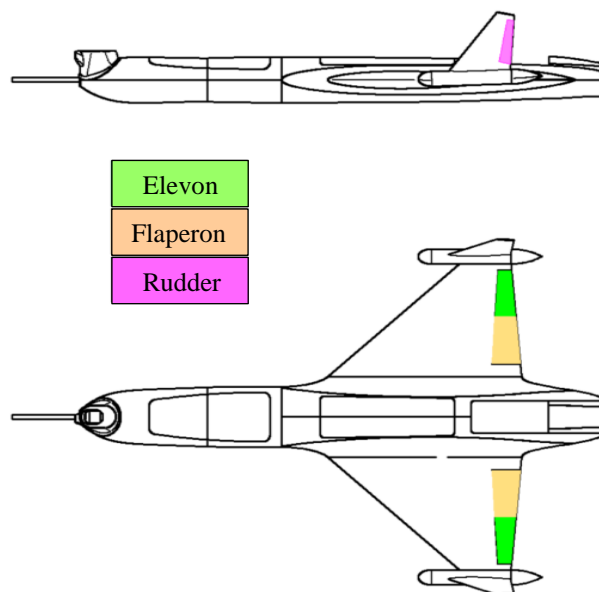


Figure 7: Flight Control Schematic

We conducted an initial aerodynamics analysis of the fuselage under experiment conditions (presented in Section 2) to learn, that a required L/D-ratio between 6-7 cannot be achieved by this configuration. The maximal achievable L/D-ratio provided by this configuration is $L/D = 10.5$. Based on this result, we searched for modifications to increase drag and decrease lift, while avoiding substantial alterations to the airframe. We identified two ways to achieve this goal: usage of air speed brakes and deployment of the landing gear during the maneuver. Further, we included the previously neglected influence of the sensor mounting, which carries optical sensors at the nose of the RLVD, into our new aerodynamics analysis. For this new analysis, we considered perturbations of the sensor mounting, use of speed brakes, and landing gear and our results show that we can achieve a final L/D-ratio of 7 by deploying the landing gear and considering the sensor mounting, which has a larger impact than initial expected. The usage of the air speed brakes is not necessary to generate this L/D-ratio.

Cameras and LiDAR sensors on the RLVD sensor mounting observe the ACCD in front and a connected data processing computer estimates the optical position feedback of the relative deviation between the ACCD and the RLVD. A communication module shares the position estimate with the ACCD. We describe these devices involved in optical position estimation in Section 4.

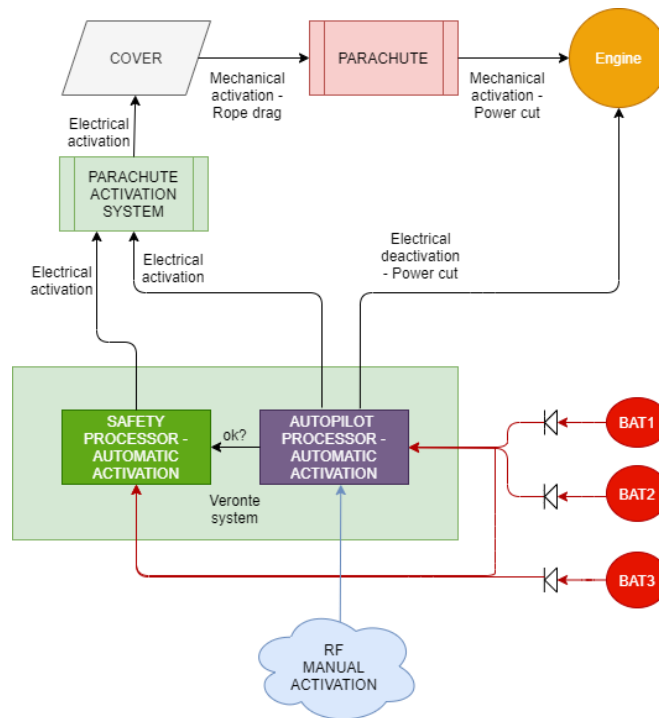


Figure 8: RLVD parachute activation system with redundant power supply and triggers to prevent single point of failures

The planned demonstration is an early phase experiment which involves a new and complex maneuver with newly designed unmanned vehicles. Thus, we expect a high probability of failure and considered measures to reduce the risk of destroying the demonstrators or harming involved participants as well as uninvolved third parties. We equipped the RLVD with an emergency parachute rescue system which is deployed as soon as the vehicle conducts any unexpected or abnormal flight behavior. The parachute can limit the area threatened by the vehicle and reduces the impact energy. The parachute system is a two staged system with a small pilot chute which is firstly deployed as an auxiliary parachute to deploy the larger main chute. The deployment of the pilot chute is ensured by a triple redundant system to avoid single point of failure. The schematic in Figure 8 describes the parachute activation system and highlights the redundant triggers to deploy the parachute.

The parachute may also be manually activated by either the safety pilot or the ground station operator. The main processor of the autopilot issues an automatic parachute deployment if any of the programmed safety margins are violated. An internal test routine, which is executed on a dissimilar safety microcontroller, monitors the main processor of the autopilot at all times during flight. Whenever the test routine identifies a malfunction of the main processor, it automatically deploys the parachute. Subsequently to parachute deployment, the engine is automatically cut off, which is either induced by the release by the parachute itself or a cut off command issued by the autopilot. We integrated three redundant power supplies to be able to provide electric power for the autopilot and parachute deployment mechanism at all times.

3.2. Towing Aircraft Demonstrator

The Towing Aircraft Demonstrator (TAD) is an unmanned experimental aircraft intended for use in research flight experiments and mission designs where a reliable fixed wing aircraft is needed to carry specific mission equipment. In opposite to the RLVD, the TAD does not reflect the aerodynamic characteristics or behaviors of a possible real towing aircraft. The focus of the TAD operations is to serve as a base for development of the required mission and flight control to implement the automatic formation flight.

The TAD is a conventional low wing cantilever monoplane of straight tapered wing with a fuselage mounted horizontal stabilizer and a pull propeller mounted in the center of the fuselage's front part. A 275 ccm two-cylinder combustion engine propels the demonstrator to a maximal velocity of 200 km/h. The landing gear is a fixed tail dragger that is designed to resist higher loads during landing and be less sensitive to uneven airfield surfaces. The MTOW of the demonstrator is 38 kg. The aircraft is a scaled replica based on the manned aircraft Edge540 which was developed for aerobatic flight. We modified the replica (additional tank volume, access, reinforcements) to meet the specifications as an experimental test demonstrator. Figure 9 shows the dimensions of the demonstrator.

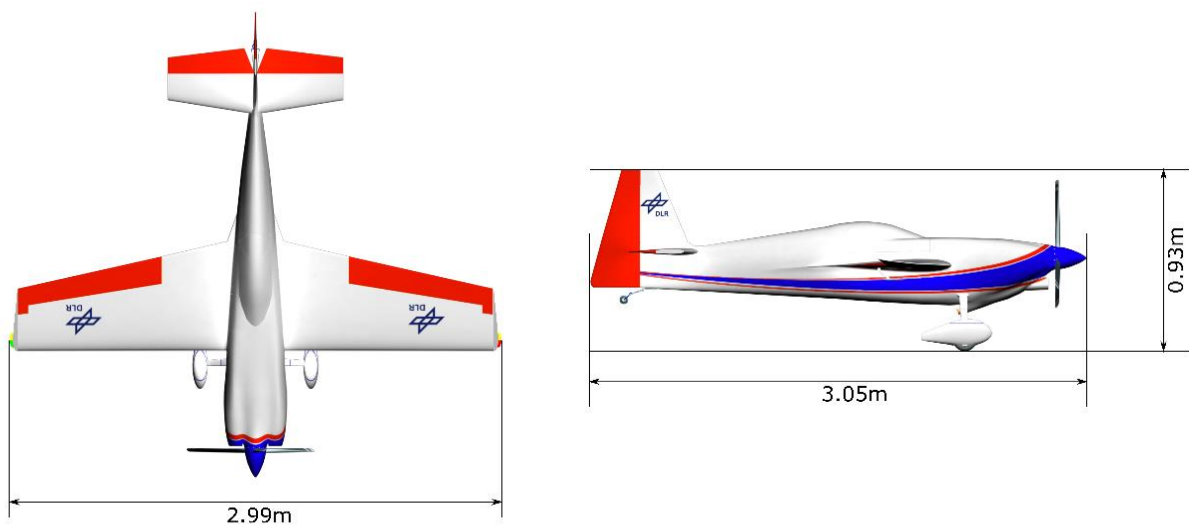


Figure 9: TAD dimension

The demonstrator is controlled by a commercial autopilot hardware of type Pixhawk 2.1 Cube which may be flashed either with our experimental software or the common open-source autopilot software ArduPilot. For missions conducted within line of sight, a purely remotely piloted backup is available which does not rely on the autopilot. The avionics and flight control servos are powered by redundant batteries and are physically separated from the mission equipment system.

3.2.1. Flight Control / Avionics

The flight control surfaces follow a conventional configuration with ailerons, elevator, rudder and flaps. Each of the surfaces is moved by a servomotor, which has a separate control channel. Engine control uses additional control channels for throttle valve, the choke, and a switch to start/stop ignition.

Figure 10 shows the basic layout of the avionics system. The control system is organized to enable the safety pilot to take manual control over all controls in case the autopilot malfunctions as long as the system is in a VLOS flight. Therefore, the system consists of a RC control segment (marked purple in Figure 10) and an autopilot system (marked orange in Figure 10).

The central control element is a central Power and Control Signal Switch (PCSS) which acts as a high reliability redundancy switch for the two input systems, the main autopilot system and backup RC control, and two battery systems. The PCSS is connected to a hardware interface panel, which is easily accessible for the ground staff to read out internal information for maintenance and search for errors. The RC backup system is used in cases the autopilot system shows unexpected behavior. The autopilot system is the standard system and provides a manual flight mode (the RC signals are passed through without processing) and several automatic flight modes like way point or automatic return to launch side operations. It is possible either manually or automatically switch between both inputs. If the RC

signal is available, the safety pilot is able to command whether the autopilot system or the backup RC system is in command of the demonstrator. Therefore, the safety pilot can take the autopilot system ‘out of the loop’, meaning that it is not considered as a possible source for the PCSS anymore. The switching between backup RC system and autopilot system is controlled by a dedicated RC channel. If the RC system’s signal is lost, the PCSS automatically switches to the autopilot system to maintain a controlled flight. The next paragraphs provide details about each of the subsystems. The RC system is kept as simple and thus robust as possible. It consists of two independent dual receivers for RC input to have four receiving signals. The receivers are linked to one radio control transmitter in the hands of the safety pilot. An 868 MHz link is used as a backup link for a 2.4 GHz link. The Received Signal Strength Indication (RSSI) decides which one to use and switches automatically.

The autopilot system consists of five main elements: two RC receivers for manual or augmented control in the same setup as mentioned as the RC System, two autopilots of Pixhawk Cube (one acts as experimental system, the other acts as backup system), a monitor to observe the condition of the experimental system, and an extended control signal switch to route the active system’s output to the central PCSS. The reason for this structure is to be able to use one autopilot to test experimental software and to have a fallback option to a reliable autopilot in a BVLOS flight as the safety pilot is not able to take control. Within VLOS flight, the default fallback option in case of autopilot failure is always the safety pilot who takes control by switching to the RC system. By default, we start our experiments with active experimental autopilot.

The autopilots are supervised by a monitoring system. In case of failure, the monitor activates the backup autopilot as a fail-safe alternative. This autopilot will then be set to a return to launch mode which guides the vehicle back to the predefined starting point. At this point, the safety pilot will regain the manual control.

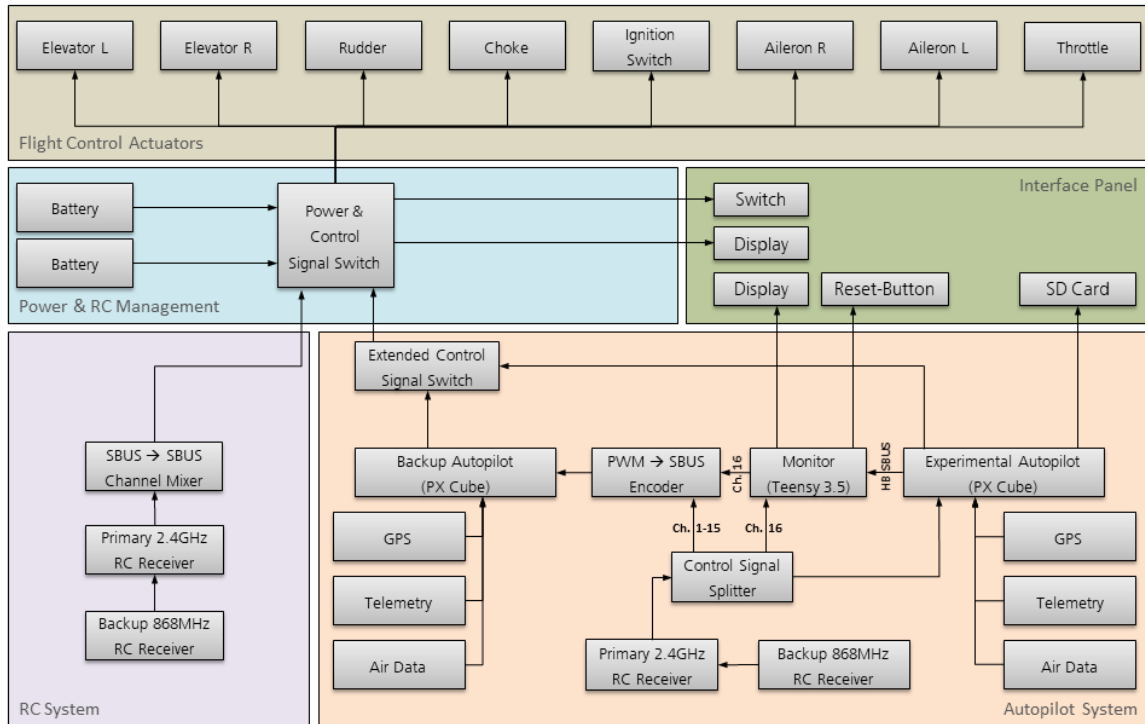


Figure 10: Avionic System Schematic

In the following paragraph, we share our defined failure modes and derived appropriate safety procedures. Then, we describe the components of the autopilot system which we designed according to the safety procedures. In this and the following paragraph, we denote the experimental autopilot expAP and the backup autopilot backAP for simplicity.

RC- link loss is an expected behavior. The RC-link has a limited range of approx. 2 km. We assume that the RC-link is only used if the aircraft is in direct visual line of sight to the safety pilot. In the case the RC-link is disconnected, a control of the demonstrator must be possible via a telemetry link.

RC-link and Telemetry loss: In this case, the autopilot must be able to detect absence of telemetry and RC-link data and initialize a predefined safety procedure starting with a loitering circle. This action bases on the assumption that the connection is temporarily interrupted and re-established after 20 s. If the link loss exceeds the time of 20 s, the autopilot

shall command a return to landing site (RTL) mission. As soon as the returning plane enters the action radius of the safety pilot, he overtakes the control and lands it immediately.

Malfunction of the primary/ experimental autopilot: Malfunction of the expAP can be either detected by the crew, based on supervision of telemetry data, or direct observation of the vehicle when in sight. In case of telemetry link loss or BVLOS flight, an onboard monitor must be provided to detect the malfunction. In the case the crew detects the failure and has the possibility to interact with the demonstrator, the safety pilot must have the power of using a manual override function to take over all vehicle's critical functions. This option must be always available when the plane is inside the pilot's action range. Otherwise, the plane is outside the action range and the ground control station (GCS) is the next crew member to act by manually switching control to the backAP to stabilize the demonstrator and to fly it back into the action range of the safety pilot. If this action fails, the onboard monitor acts as the last safety layer by detecting the failure and the absence of a crew reaction, which could be caused by a link loss or significant communication delay, and the monitor switches automatically to the backAP. For this case, backAP must have a pre-implemented standard safety procedure to follow so it can fly the demonstrator back to the location of the crew.

Unexpected behavior of demonstrator and demonstrator does not react on predefined exception handling. e.g. no possibility to interact with autopilots or monitor: In this case, all the above-mentioned safety layers fail and we abort the flight test with an independent termination link to interrupt the engine's ignition and deploy the rescue parachute system (see Section 0).

In the following, we present details about the subsystems experimental autopilot, backup autopilot, and monitor inside the autopilot systems. We designed these systems based on the aforementioned failure modes.

The **Backup Autopilot System** (backAP) is an unmodified commercial off-the-shelf (COTS) Pixhawk 2.1 Cube. This autopilot is used by a large private and commercial community which sustains a continuous improvement process for the Pixhawk's autopilot software. Therefore, we consider the unmodified system to be very reliable. The Pixhawk includes a Flight Control Unit (FCU), onboard logging, C2Link interface and protocol, power management, and multiple integrated sensors. These sensors include GNSS, two inertial sensors, a pressure sensor, and a magnetometer. The autopilot is used for manual and automatic flight control. It can run various versions of flight control software. We use the ArduPilot Flight Control Software (FCS) for the TAD aircraft. The backup autopilot is connected to a power hub of the PCSS and therefore powered by redundant batteries. The ArduPilot software has a return-to-home function which is able to guide the demonstrator back to a home point. Prior to each flight experiment, we ensure that the home point is placed where the crew is located and known to the backAP.

The basic **Experimental Autopilot System** (expAP) is generally identical with the hardware of the backup system. We added further sensors (airspeed sensor, RPM sensor, Engine temperature sensor, fuel flow, and fuel capacity sensor) that are not necessarily part of the Pixhawk environment developed by the Pixhawk community. In contrast to the hardware, the software is not COTS, but bases on long-term DLR in-house development and research.

The software implemented controller module uses a model-based flight control and the software module can be easily transferred into a software-in-the-loop simulation environment. The simulation environment is implemented in Matlab/Simulink and bases on the Paparazzi Fixed Wing controller, one of the earliest open source flight control projects. We ported the Paparazzi controller structure to a model-based design. The original Paparazzi controller module consists of a cascaded control with an inner loop for attitude and an outer loop for navigation control, which we enhanced with a speed PID loop and small adaptations of the attitude loops for feedforward gains. These changes provide a direct transfer of tuned parameters from an ArduPilot system to this experimental controller.

The **Monitoring system** evaluates whether the telemetry and the output to the servos of the experimental autopilot are valid. The monitor observes the Pixhawk's heartbeat message¹ and the state of the control signals of the expAP to decide whether the system is in normal operation or not. In case one of the signals is lost for a defined time period or invalid, the monitor assumes an error within the expAP and commands the backup system to take control. Furthermore, also the failsafe and Lost-Frame flags of the control signal packages are monitored because they also provide indicators of probable failures.

If the backAP detects the activation signal of the monitor, a mode change is triggered and sets itself into a return-to-home mode. The swapping to the backup system can also be commanded via the ground control station (GCS) which is connected to the backAP via telemetry link. The monitoring system has its own logging for post-flight analysis and a control display to check its status on ground. While airborne, we check the monitor status via the GCS.

Note, the monitoring system itself is part of our research and thus a part of the experimental system. Thus, we implemented a fail-safe which automatically switches control to the backAP, in case the monitor becomes faulty and stops working.

¹ The heartbeat message is a timed message, which is broadcasted in intervals of one second, to ensure that the Pixhawk is operational.

3.2.2. Parachute Rescue System

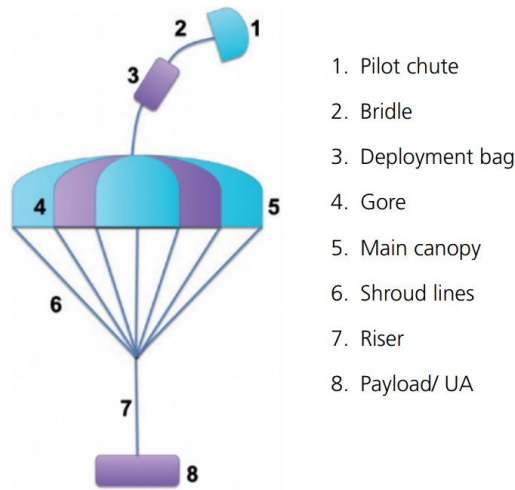


Figure 11: Concept of two-stage Parachute Deployment

The main purpose of using a parachute system is to add an additional layer of safety in case of an emergency or malfunction. The parachute rescue system is not intended to rescue the aircraft without damaging it, but to limit any influence or damage to uninvolved third parties to an acceptable level and to limit the affected area by preventing a fly away of the demonstrator. The rescue system in use was developed by DroneRescue [11] in cooperation with the DLR. The rescue system deploys in two stages. A pilot chute deploys first and unfolds the main chute's canopy. This approach has two advantages. First, it is easier to integrate the system into the demonstrator's fuselage as the main chute and pilot chute are separated from each other. Second, the two staged deployment process significantly reduces shock-load force produced by the unfolding of the main chute. The shock load is the initial force emerging when the canopy is inflated with air which causes a strong traction to the aircraft fuselage at the parachute attachment point. The concept of the two-stage deployment is shown in Figure 11. The main chute's canopy is connected to the aircraft via shroud lines and four risers (in opposite to the concept sketch). In this application, all shroud lines end on a single end of the risers, whereas the riser attaches to the fuselage in four attachment points. We located the riser's attachment points to be on loadbearing structures like the wing spars of the aircraft fuselage. The shroud lines are covered by a slider to delay the opening process of the main canopy to take a longer time period, which additionally reduces the maximum shock load.

The release of the parachute rescue system occurs via datalink, which is independent to the telemetry and RC datalinks. The datalink uses the SRD-band at a frequency of 868 MHz and an output power of up to 500 mW. This specification is combined with a data protocol especially designed for low traffic long range communication. During the non-active operation, the datalink only observes its own signal and system health and thus can be operated with a narrow bandwidth, which allows long-range communication. In a case of activation, the transmitted signal switches a relay which deploys the parachute and cuts off the engine.

3.2.3. Winch

The Winch is mounted under the fuselage of the towing aircraft and is centered between the main landing gear. This location is close the COG of the aircraft and therefore the lever arm and the movements of the ACCD and the towing rope have little influence on the demonstrator. The winch was developed and manufactured by DLR and carries approx. 30 m of rope. The winch is motorized and equipped with controller that allows a relative length control of the rope length. The ACCD controller computes and commands the target values for the rope length. We use a 433 Mhz datalink for the communication between the ACCD and the winch (see Figure 3).

3.3. Aerodynamically Controlled Capturing Demonstrator

The main body of the Aerodynamically Controlled Coupling Device (ACCD) bases on a trailing cone to achieve a stable flight behavior. We equipped the cone with a control system to enable vertical and lateral motion orthogonal to the towing aircraft's longitudinal axis x_b . We designed the control surfaces to be capable of moving the drogue in the range of at least $-/+2$ m in each direction to compensate for position offsets of the TAD and RLVD, which result from atmospheric turbulences and deviations from the flight path induced by GNSS inaccuracies. Moreover, changes in

heading ψ_{ACCD} and pitch θ_{ACCD} should be minimized to achieve a steady orientation with respect to the formation for applying the necessary control commands for the vertical or lateral adjustments. For the principal purpose of testing the vertical/lateral motion, we implemented simple roll stabilization. The equipment of the device is stored in the center body of the ACCD to have a small moment of inertia around the roll axis.

For the experimental analysis of the IAC method with smaller unmanned aircraft, we build an experimental prototype of the ACCD. The setup of the ACCD is described in the following sections. Due to the thrust limitations of the towing aircraft, the weight of the ACCD should not exceed 1.0 kg. Also, future modifications, such as an adaptation of the size of the control surfaces or the trailing cone, should be possible without redesigning a completely new ACCD. Consequently, the prototype was realized as a modular structure using rapid prototyping approaches. The main components are: the fuselage with avionics, servo motor support, and coupling to the towing rope, the trail cone, and the control surfaces. Figure 12 shows a 3D model and Table 1 presents some system parameters of the ACCD.

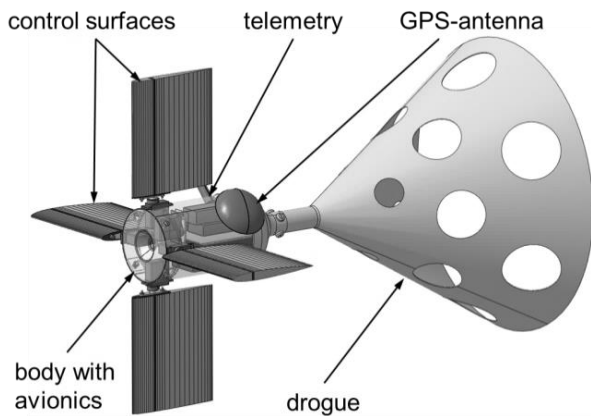


Table 1: System parameters of the ACCD

length	≈ 450 mm
cone diameter	370 mm
weight	650 g
control surface span	120 mm
control surface width	100 mm
max. control deflection	$\pm 45^\circ$

Figure 12: Isometric View of the ACCD

The control surfaces are oriented in a vertical and horizontal direction. This orientation enables the ACCD to directly deflect into orthogonal directions relative to the towing aircraft by using only one pair of surfaces per direction. The control surfaces are mounted directly on the axis of the actuators, so that the installation is very direct and space-saving. This approach requires to limit the loads on the control surfaces to keep the bending moments on the servo axes within the limits of the servo. The drawback of this limitation is a decrease of the ACCD's agility.

The servo motor installations are designed to allow for the quick replacement of damaged parts and have a predetermined breaking point to protect the center body which holds the avionics. An additional release servo allows for quick decoupling of the ACCD from the towing aircraft in case of failure. To minimize turbulence in the cone, it was built with holes, which direct flow energy into the wake space inside of the cone, which is similar to the design of trailing cones for pressure measurements.

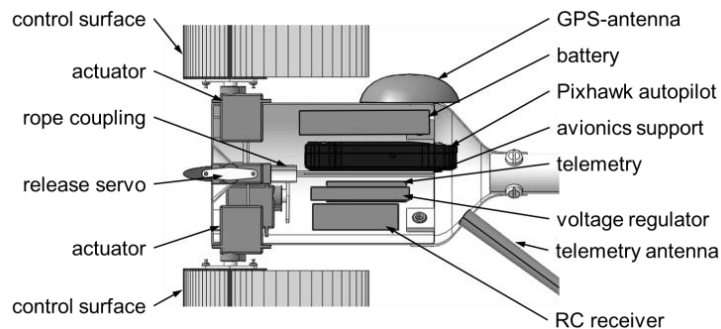


Figure 13: Avionics Integrated in the ACCD (Section View)

For the flight control, we used a similar approach as for the flight control software in the TAD. As we face stronger weight limitations on the ACCD, we use a Pixhawk 4 as autopilot instead of a Pixhawk Cube. The controller bases on DLR research and we implemented it in Matlab/Simulink. The controller is a part of the PX4 Framework which we presented in Section 3.2. The ACCD has two telemetry links, that connect it to the GCS and the winch mounted to the TAD. The datalink operates over a 433 MHz frequency band with 100 mW transceivers at both ends. Figure 13 shows a section view of the ACCD and the main avionic components installed there. We collected first results about the

ACCD’s performance in exemplary flight tests at which we manually controlled the ACCD to move +/- 3m orthogonally to its body fixed x-axes at a horizontal speed of 100 km/h. We assume, that the ACCD will achieve the same performance at the planned demonstration velocity of 150 km/h. Final certainty about the ACCD’s control and trim abilities will be available after the flight test campaign.

4. Environment perception

As mentioned in Section 2, the IAC maneuver has two parts, the rough and the fine formation phase. The rough formation has the aim to set the scope for the fine operation. The rough formation bases on Kalman filter-based sensor fusion of commercial off-the-shelf GNSS and inertial sensors on TAD and the RLVD. The TAD starts to align its position and velocity the RLVD as soon as they are 30 m apart. The RLVD publishes its position and velocity to the TAD to enable this operation. The assumed accuracy for this operation is round about 1-5 m, depending on the external environment situation. Once the rough formation is established, it enables the optical sensors used for fine formation to take over the alignment process. It is planned that these sensors work in a range up 20 m with an accuracy of 0.5 m. At the contact range (1 m ahead the sensors), we expect an accuracy of 0.1 m.

For the final approach, we use two independent optical sensors that work in the near infrared (NIR) band and provide a real time relative position estimate between ACCD and RLVD. This redundancy ensures the maneuver can be completed in case one sensor is not available. Using NIR light has the advantage of being less susceptible to background noise in the image, mainly because light in the NIR band coming from the sun is blocked in the upper layers of the atmosphere.

Infrared light has the additional advantage of better penetration in misty conditions or clouds. Low visibility in misty conditions is due to refraction of light on tiny water droplets suspended in air. Refraction redirects light in a chaotic way, effectively blurring out the object behind the mist. The refractive index of water depends on the wavelength [12] [13] [14] with lower indexes at higher wavelengths. Refractive indexes near the index of surrounding air limit the effect of misty conditions. Therefore, low indexes are preferable. The disadvantage of slightly higher absorption of IR-light in water (compared to visible light) can be compensated easily by higher emission.

4.1. Camera perception

The camera-based position estimation uses an active marker-based tracking technology. Therefore, the inside of the ACCD cone is equipped with seven NIR LEDs which are placed in a specific pattern (see Figure 14). Each LED emits light with 850 nm and 2.5 W. This configuration is not eye safe because of the relatively high emit power and the light cannot be detected by human eyes with the consequence that the human lid closure reflex is not triggered. The resulting pattern is recorded by an NIR sensitive camera, which is equipped with $f=25$ mm lens and a narrowband optical filter for wavelengths between 820 nm - 910 nm to exclude possible disturbances.

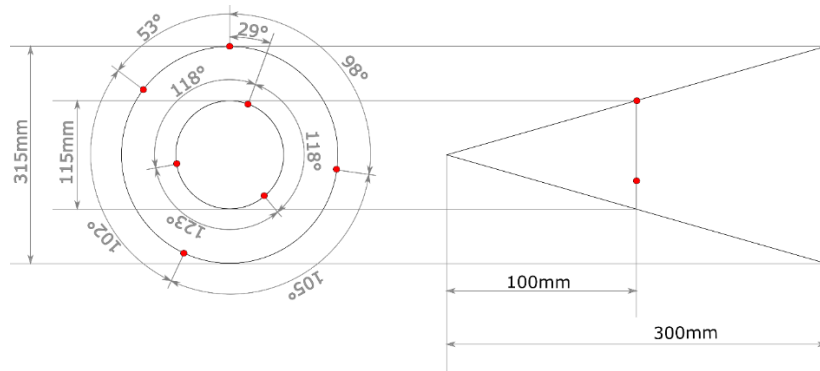


Figure 14: Mounting of LEDs in the inside of the ACCD cone.

After recoding the NIR-LED pattern with the camera, threshold filters and a blob-detector detect the LEDs. Figure 15 shows an example camera image of the NIR-LEDs inside the ACCD cone as seen from the RLVD. In a second step, the detected LEDs inside the image plane are assigned to their correspondent position in the 3D pattern, which enables the estimation of the three-dimensional pose of the ACCD cone in the last step. We use the Perspective-n-Point (PnP) algorithm [15] to estimate the full pose of the ACCD (position and orientation) when more than three LEDs are visible. In the case only three LEDs are visible, we use a P3P algorithm [16] to compute the 3D position of the cone without its orientation. If less than three LEDs are visible, an estimation of the ACCD pose or position is not possible. We also

implemented a tracking of the estimated ACCD pose within the camera coordinate system to cover short periods in which an estimation is not possible. We use a simple Kalman filter for the tracking.



Figure 15: NIR-LED pattern, visible in the cone of the ACCD in static camera tests

4.2. LiDAR perception

The LiDAR (Light Detection and Ranging) sensor is used to detect the position of the ACCD in relation to the RLVD. The used LiDAR system is a three-dimensional laser scanner that takes several distance measurements to build up a three-dimensional image of the surrounding environment. The distance measurement is a time-of-flight measurement of a light pulse, which is measured between the active pulse emission and the detection of its echo after reflection at an obstacle's surface. The distance between the light source and the obstacle surface is calculated based on the measured time interval and the constant speed of light. If several beams are transmitted from a known origin in different, but known directions, a three-dimensional distance image of the surrounding environment can be estimated. The described operation principle is used by several COTS devices on the market. We use an Ouster OS1-64 which provides a field of view of $45^\circ \times 360^\circ$ with a vertical resolution of 0.35° - 2.8° and horizontal resolution of 0.35° up to a range of 120 m.

The processing algorithms use the Robotic Operating System (ROS) as middleware to acquire the data of the LiDAR. The output of the initial processing contains several 2D images that contain range and reflectivity values as seen in Figure 16 and Figure 17. The detection assumes that the ACCD is uniquely identifiable based on its physical properties. These properties are the reflectivity of its surface and the shape of its projection on the image plane.



Figure 16: Range image from Ouster OS1-64



Figure 17: Reflectivity image from Ouster OS1-64

The ACCD fuselage was built using a rapid prototyping process with white PLA filament. The material of the cone however is a black carbon fiber composite. Based on this setup, we assume, that the reflectivity of the cone inside is not unique and several objects in the surroundings will have a comparable reflectivity and a unique identification is not possible. This problem was accounted by coating the inside of the cone with a micro prism coating. The coating reflects incoming light back in the same direction where it comes from and works as a passive reflector as known from traffic signs. With this setup the incoming LiDAR beams are directly reflected to the LiDAR where a high-level reflectivity can be detected. As shown in Figure 17, the cone is the brightest object in the image even in comparison to bright stainless-steel objects on the left-hand side of the cone. Therefore, the reflectivity of this modified cone can be assumed unique, in a natural environment.

The second feature is the shape of the ACCD in the sensor data. The observing sensors are mounted on the RLVD which flies behind the ACCD in formation. Based on the rough formation flight, it can be assumed, that in nearly all observations of the ACCD the cone is covering its avionics compartment and control surfaces and thus always appears to be elliptically or circularly shaped.

The first step of the detection algorithm is to analyze the reflectivity data of the LiDAR. This data is available as an ordered matrix like a camera image. Therefore, OpenCV methods can detect the highest values in reflectivity data. After a validation that the detected shape corresponds to a circular/ellipsoid shape, the identified reflectivity data are combined with the corresponding range data to finally calculate the three-dimensional position in relation to the LiDAR origin.

4.3. Sensor Data Fusion

As mentioned in Sections 4.1 and 4.2, the RLVD is equipped with two perception sensors: the camera and the LiDAR. Additionally, a small laser range finder is attached to the tip of the nose boom, which mainly serves the purpose of detecting contact between ACCD and RLVD. As part of the general avionics system, the ACCD and the RLVD are both equipped with GNSS and INS sensors to estimate the respective state. Both states are also available in the perception unit of the RLVD. Thus, we can utilize all this information to find a good relative position estimate of the ACCD. Fusion of the information requires an algorithm which combines all available measurements into one state for the ACCD and weighs them according to their quality. The sensor measurements are subject to noise and delay, which depend on the form of post processing and data transmission. Additionally, they arrive at different times and are sampled with different sample times, as shown in Figure 18.

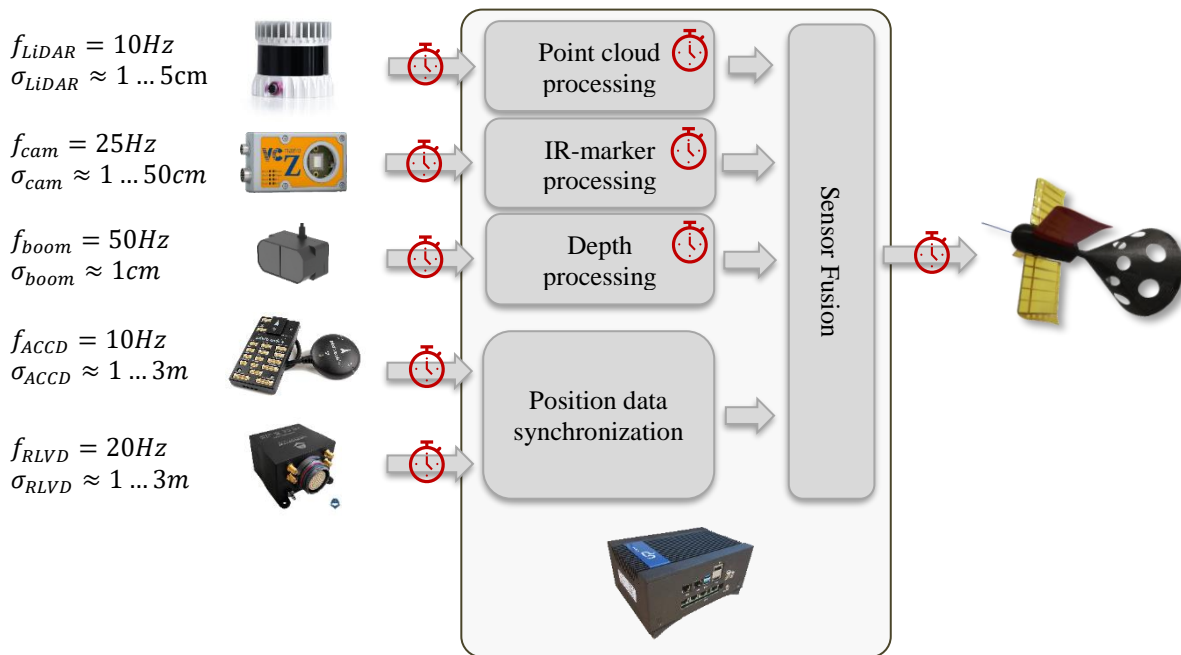


Figure 18: Sensor Fusion Problem Overview

The data acquisition rate of the camera is relatively high, which allows relatively fast processing of images, whereas the GNSS based position estimates of the autopilots arrive with a lower frequency due to the limited maximum bandwidth of the datalinks. The measurement frequency in general depends on the respective sensor acquisition rate, individual processing time, and on the datalink bandwidth. Therefore, it is possible that several measurements are available in the same time step while some time steps hold no new information.

Additionally, the quality of the measurements differs substantially. While the LiDAR provides a good depth measurement, the cartesian position error in the LiDAR body-fixed x-y-plane grows quadratically with greater distance in the z-axis. In case of the camera measurement, the depth itself has quadratic error characteristics. We calculate the relative GNSS based position measurement by subtracting the RLVD position from the ACCD position. Thus, the variances of both individual measurements must be summed up as they are assumed to be stochastically independent. The overall goal of the sensor fusion algorithm is to provide the ACCD with a position estimate relative to the RLVD nose boom contact point, which then can be used by the control algorithm of the ACCD to minimize the deviation. A common approach to fuse noisy measurements in the time discrete domain is to use a Kalman filter. By taking a given

linear state space model and all measurements from the past into account, the state is recursively estimated. The linear state space model of the dynamics must satisfy the condition of observability. There are also extensions available for nonlinear process and observation models like the Extended or Unscented Kalman filter. In our case, we used an Extended Kalman filter for state estimation.

To deal with delayed measurements, the standard equations of the Extended Kalman filter must be slightly adapted. The general idea is to correct a previous measurement estimate based on an old state vector with the delayed measurement and to apply the corrections to the current state. Therefore, the state vector, covariance matrix and the input are saved in a buffer. In this procedure, some simplifications are applied, so that the estimated state will only be semi-optimal. These simplifications are made to save computing time and available memory. The updated estimation equations are based on [17]. Since the measurements arrive at different time intervals, the estimation is decoupled from the propagation. Whenever multiple measurements arrive at the same time, the observation and measurement noise matrices are respectively concatenated into one larger matrix. While the propagation is run with a fixed frequency of 50 Hz, the estimation step will only occur if a measurement is available. The noise matrices are scaled accordingly regarding to the respective time intervals.

4.3.1. Filter Modelling for IAC

In a first approach, we chose a simple 3D-point mass model which is capable to propagate the state for a short time interval without any available measurements. The estimated state is susceptible to periodic oscillations of the real position as the velocity and acceleration, which are not directly measured, must be corrected in a first step. The resulting phase delay depends heavily on the magnitude of the entries in the process noise matrix \mathbf{Q}_k . An alternative approach would be to model the position as a random walk process. The value of the estimated position only changes if a measurement is received in the estimation step and depends heavily on the quality of the measurement. In this case, the behavior of the Kalman filter is comparable to that of a low-pass filter. It is also possible to include the closed loop system dynamics of the ACCD into the process model of the Kalman filter. However, this procedure requires good process knowledge and a relatively simple control law, which can be easily represented in the state space model. This is not the case for the highly nonlinear system dynamics of the tethered ACCD used in the IAC-maneuver.

The state vector includes the relative position, velocity, and acceleration in the flight-path coordinate system (k-frame). The acceleration is modelled as random walk process. Euler angles $\boldsymbol{\varphi}$, flight-path azimuth χ , and the angle of climb γ are the inputs of the state space model. They are only necessary for the observation model. Thus, the input matrix \mathbf{B}_k is empty. We have

$$\mathbf{x}_k = \Delta(\mathbf{p}_k \quad \mathbf{v}_k \quad \mathbf{a}_k)_k^T \quad (1)$$

$$\mathbf{u}_k = (\boldsymbol{\varphi} \quad \chi \quad \gamma)_k^T \quad (2)$$

The linear state transition matrix is given by

$$\mathbf{F}_k = \mathbf{A}_k = \begin{pmatrix} \mathbf{1} & dt & 1/2 dt^2 \\ \mathbf{0} & \mathbf{1} & dt \\ \mathbf{0} & \mathbf{0} & \mathbf{1} \end{pmatrix} \quad (3)$$

The observation models are given by the following equations, where \mathbf{y}_k are the measurements, \mathbf{R}_b^{Sens} , \mathbf{R}_k^b , \mathbf{R}_k^g , \mathbf{R}_b^g are rotation matrices, where the lower index describes the “from” and the upper index the “to” coordinate system, \mathbf{r}_b^{boom} is a rotation vector, the first row of the respective rotation matrix, and \mathbf{d}_b^{Sens} are the mounting positions of the sensors with respect to the center of mass of the RLVD. We have

$$\mathbf{y}_k = h(\mathbf{x}_k, \mathbf{u}_k) \quad (4) \quad d_{boom} = \mathbf{r}_b^{boom}(\mathbf{R}_k^b \mathbf{p}_k - \mathbf{d}_b^{boom}) \quad (7)$$

$$\mathbf{p}_{LiDAR} = \mathbf{R}_b^{LiDAR}(\mathbf{R}_k^b \mathbf{p}_k - \mathbf{d}_b^{LiDAR}) \quad (5) \quad \text{Autopilot} \begin{cases} \Delta \mathbf{p}_g = \mathbf{R}_k^g \mathbf{p}_k - \mathbf{R}_b^g \mathbf{d}_b^{AP} \\ \Delta \mathbf{v}_g = \mathbf{R}_k^g \mathbf{v}_k \end{cases} \quad (8)$$

$$\mathbf{p}_{cam} = \mathbf{R}_b^{cam}(\mathbf{R}_k^b \mathbf{p}_k - \mathbf{d}_b^{cam}) \quad (6) \quad \text{Autopilot} \begin{cases} \Delta \mathbf{p}_g = \mathbf{R}_k^g \mathbf{p}_k - \mathbf{R}_b^g \mathbf{d}_b^{AP} \\ \Delta \mathbf{v}_g = \mathbf{R}_k^g \mathbf{v}_k \end{cases} \quad (9)$$

Most of the rotation matrices have a dependency to the input of the state space model. As example \mathbf{R}_k^g can be derived from the flight-path azimuth and the angle of climb, \mathbf{R}_b^g is calculated from the Euler angles, and \mathbf{R}_k^b can be calculated by multiplying both matrices: $\mathbf{R}_k^b = \mathbf{R}_b^{gT} \cdot \mathbf{R}_k^g$ [18].

The decision to choose the flight-path coordinate system in the state vector is based on the advantage that high frequent oscillations in the angular velocity of the RLVD only have minor effects on the relative position difference. Furthermore, side slip conditions due to crosswinds are already accounted for when choosing the position in the flight-path coordinate system as process variable in the position controller of the ACCD.

4.3.2. Simulation Results

To test the sensor fusion algorithms before running them on the hardware in flight tests, we use our simulation framework based on MATLAB[®]/Simulink[®] [19]. It consists of all modules from the overall scaled flight test setup including the flight mechanical simulation of the three demonstrators (TAD, ACCD, and RLVD) and the required submodules like sensor, datalink, environment, winch, and rope models. The C++ code is directly injected into the simulation by using the built-in s-function builder. As the C++ code is originally deployed in a ROS framework [20], the coordinate systems are following different conventions. Thus, we implemented several wrapper functions that transform the quaternions and coordinates from NED (North-East-Down) to ENU (East-North-Up) and FRD (Front-Right-Down) to FLU (Front-Left-Up).

To test the sensor fusion algorithm, the respective input values need to be provided. Therefore, we use sensor models to generate noisy measurements. The sensor models generically simulate each sensor's whole processing path, consisting of acquisition, processing, and data delivery. The actual data processing of each sensor is not simulated. Additionally, we simulate datalinks by delaying and corrupting data. Table 2 lists the values used in our simulation:

$$dt = 0.02 \text{ s}, \quad \mathbf{Q}_k = dt \cdot \begin{pmatrix} 0.001 & 0 & 0 \\ 0 & 1 & 0 \\ 0 & 0 & 25 \end{pmatrix} \quad (10)$$

Table 2: Characteristic values of sensors used in simulation

	Camera	LiDAR	Nose Boom LiDAR	Autopilot (GNSS)	
				Position	Velocity
f (HZ)	25	10	50	10	
T_d (s)	0.04	0.02	0.02	0.1 (datalink delay)	
σ -Depth (m)	$0.002 \cdot d^2$	$0.001 \cdot d + 0.007$	$0.01 \cdot d$		
σ -Pan/Tilt ($^\circ$)	0.5	Hor.: 0.03 / Vert.: 1			
σ -Hor./Vert.				3 / 5 (m)	3 / 5 (m/s)

Figure 19 to Figure 22 depict the results from a closed loop simulation run in close formation. The maneuver starts with an initial distance of 50 m between RLVD and ACCD which is steadily reduced. After round about 60 s of simulation time, the ACCD comes so close to the nose of the RLVD that it disappears out of the FOV of the camera and LiDAR sensors. In consequence, the sensor fusion algorithm relies only on noisy GNSS based measurements from the autopilots, which cause large errors in the estimated state. Figure 19 shows the relative position estimate compared to the ground truth value calculated from undisturbed states of the flight mechanical models. Additionally, the sensor measurements transformed into the path coordinate system are depicted as well. For better visibility only every 5th measurement value is drawn. Figure 20 pictures the estimated velocity and acceleration. The legend drawn in the upper left corner of Figure 19 also applies to this figure. As can be seen on the top left plot, the derivatives of the position have a phase delay of round about 0.2 s. In case of the acceleration, which was modeled as random-walk process, the filter acts like a low pass filter. This behavior results from the simple 3D-point-mass modelling approach and relatively low gains in the system noise matrix.

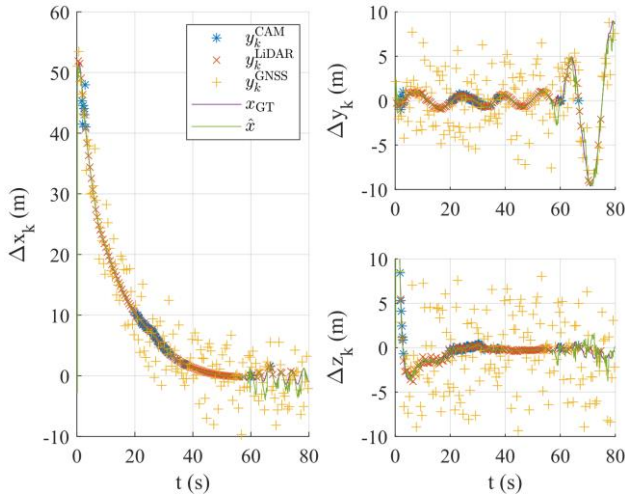


Figure 19: Estimated Position and Ground Truth (GT) (only every 5th measurement is shown)

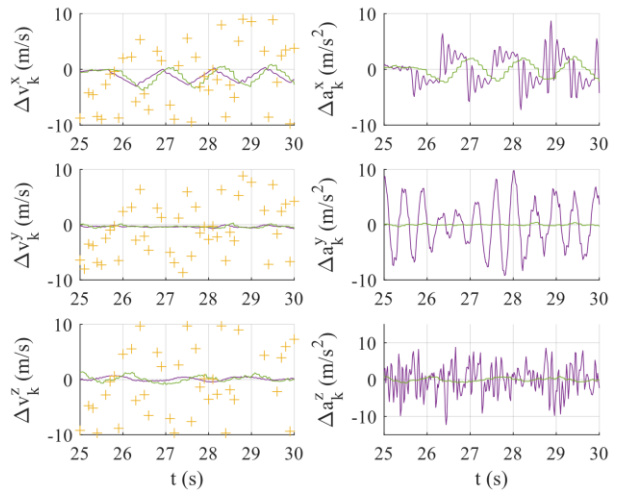


Figure 20: Estimated Velocity, Acceleration & GT

Figure 21 and Figure 22 show the position and measurement errors with respect to the ground truth values. The legend drawn in the upper right corner applies to both of the aforementioned figures. The position error shrinks with a smaller distance between RLVD and ACCD due to the better quality of the measurements. For distances below 10 m, as depicted in Figure 22, the standard deviation of the relative position error of the estimate for the x and z-axis is about 4 cm. For the y-axis, the standard deviation equals 1 cm. However, this accuracy only applies if the ACCD is in the field of view of at least one of the vision-based sensors. If the sensor fusion algorithm must rely on the relative position estimate of the autopilots, the position error grows to values above 2 m. This could be resolved by using RTK GNSS and tightly coupled sensor fusion strategies instead of loose coupling as applied here. However, in the real experiment the pitch of the sensors will be adjusted so that the ACCD will always be in the FOV of at least one of the vision-based sensors.

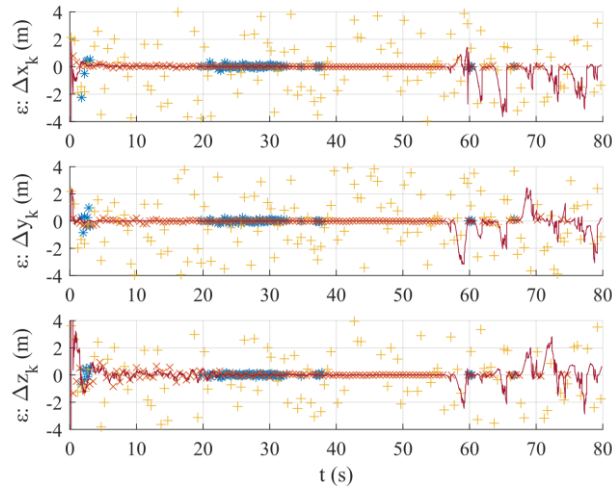


Figure 21: Position & Measurement Error (only every 5th measurement is shown)

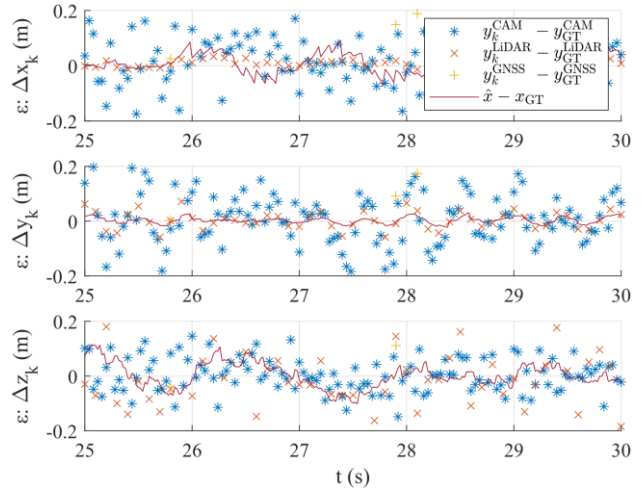


Figure 22: Position & Measurement Error (close-up)

To overcome the problems of increasing phase delay in the derivatives and in the position itself, a more accurate state space model incorporating ACCD flight mechanics will be tested in the future. In addition, alternative sensor fusion techniques such as moving horizon estimation (MHE) will be investigated.

5. Conclusion/ Outlook

The presented work gives an overview of planned scaled operation of an In-Air-Capturing maneuver, which will be implemented in the project FALCon, funded by the EC. A goal of the FALCon project is to validate the feasibility of the IAC concept with the scaled setup and to generate general statements for an implementation of an actual In-Air-

Capturing Maneuver to recover a winged booster rocket stage. For the scaled implementation, we presented the mission setup with the local circumstances of the test area, the tree involved demonstrators for towing aircraft, reusable rocket launch vehicle, and coupling device, with the focus on safety functions, and the installed environment perception system. The environment perception system is mounted on the reusable launch vehicle demonstrator and is required for the final phase of the IAC-Maneuver. The presented work gives a first glance on our research topics and shows the work in progress.

Ongoing work focuses on obtaining the permission to conduct flight experiments with the scaled demonstrators from the responsible authorities. Then, we will conduct the flight experiments at the National Experimental Test Center for Unmanned Aircraft Systems in Cochstedt, Germany. The implementation of the flight tests will be an iterative process from simple flights of the single demonstrators in sight to validate their behavior and our safety concepts, over tests that are done beyond the visual line of sight, up to final joint flight tests of all three demonstrators. In the second half of 2022, the FALCon project will end and it is the aim, that all flight tests are done until this date.

6. Acknowledgements

Part of this work was performed within the project ‘Formation flight for in-Air Launcher 1st stage Capturing demonstration’ (FALCon) addressing development and testing of the “in-air-capturing” technology. FALCon, coordinated by DLR, is supported by the EU within the Horizon2020 Program 5.III. Leadership in Enabling and Industrial Technologies – Space with EC grant 821953. Further information on FALCon can be found at <http://www.FALCon-iac.eu>.

We thank all our colleagues who supported us during the investigations and the ground and flight test campaign. Special thanks go to our safety pilots David Peters and Michael Kislat-Schmidt. In addition, we want to also thank the colleagues from the companies Soft2Tec, Germany, which developments parts of the environment perception system and DroneRescue, Austria, which design the rescue parachute system for both demonstrators. Finally, we want to thank our team members Lennart Kracke and Thorben Bornscheuer for their support.

7. References

- [1] SpaceX, [Online]. Available: <https://www.spacex.com/reusability-key-making-human-life-multi-planetary>. [Accessed 04 12 2019].
- [2] S. Stappert, "Systematic assessment of RLV return methods," in *VKI Lecture Series - In-air-capturing device and reusable launchers*, Sint-Genesius-Rode, Belgium, von Karman Institute for Fluid Dynamics, 2022.
- [3] M. Sippel, J. Klevanski and J. Kauffmann, "Innovative Method for Return to the Launch Site of Reusable Winged Stages," in *52nd International Astronautical Congress*, Toulouse, 2001.
- [4] M. Sippel, S. Stappert, L. Bussler, S. Krause, S. Cain, J. Espuch, S. Buckingham and V. Penev, "Highly Efficient RLV-Return Mode “In-Air-Capturing” Progressing by Preparation of Subscale Flight Tests," in *8th EUROPEAN CONFERENCE FOR AERONAUTICS AND SPACE SCIENCES (EUCASS)*, Madrid, 2019.
- [5] S. I. Purdy, "Probe and Drogue Aerial Refueling Systems," in *Encyclopedia of Aerospace Engineering*, John Wiley & Sons, Ltd, 2010.
- [6] S. Cain, S. Krause and J. Binger, "Entwicklung einer automatischen Koppereinheit für das Einfangen einer wiederverwendbaren Trägerstufe im In-Air-Capturing," in *German Aviation and Space Congress*, München, 2017.
- [7] S. Krause and S. Cain, "UAV Pre-Study for In-Air-Capturing Maneuver," in *IEEE Aerospace Conference*, Big Sky, USA, 2022.
- [8] M. Sippel, "Introduction to the LS and FALCON systems definition and requirements," in *VKI Lecture Series - In-air-capturing device and reusable launchers*, Sint-Genesius-Rode, Belgium, von Karman Institute for Fluid Dynamics, 2022.
- [9] M. Sippel, "FALCon," German Aerospace Center, [Online]. Available: <https://www.falcon-iac.eu>. [Accessed 10 05 2022].
- [10] Embention, "Autopilot 1x," [Online]. Available: <https://www.embention.com/product/autopilot-for-drone/>. [Accessed 21 04 2022].
- [11] DroneRescue, [Online]. Available: <https://dronerescue.com>. [Accessed 23 05 2022].
- [12] IAPWS 5C, "Release on the Refractive Index of Ordinary Water Substance as a Function of Wavelength, Temperature and Pressure," CNEA, Dr. Roberto Fernández-Prini, Argentina, 1997.

- [13] D. L. a. W. Livingston, *Color and light in nature*, Cambridge University Press, 2001 (2nd ed.).
- [14] D. Segelstein, "M.S. Thesis: The Complex Refractive Index of Water," University of Missouri, Kansas City, 1981.
- [15] E. Marchand, H. Uchiyama and F. Spindler, "Pose Estimation for Augmented Reality: A Hands-On Survey," *IEEE Transactions on Visualization and Computer Graphics, Institute of Electrical and Electronics Engineers*, pp. pp.2633 - 2651, 2016.
- [16] X.-S. Gao, X.-R. Hou, J. Tang and H.-F. Cheng, "Complete solution classification for the perspective-three-point problem.," *IEEE Transactions on Pattern Analysis and Machine Intelligence*, p. 25(8):930–943, 2003..
- [17] J. Wendel, *Integrierte Navigationssysteme - Sensordatenfusion, GPS und Inertiale Navigation*, 2 ed., München: Oldenbourg Wissenschaftsverlag GmbH, 2011.
- [18] R. Brockhaus, W. Alles and R. Luckner, *Flugregelung*, 3 ed., Springer-Verlag Berlin Heidelberg, 2011.
- [19] J. C. Dauer and S. Lorenz, "Modular Simulation Framework for Unmanned Aircraft Systems," in *AIAA Modeling and Simulation Technologies Conference*, Boston, USA, 19.-22. Aug. 2013.
- [20] M. Quigley, K. Conley, B. Gerkey, J. Faust, T. Foote, J. Leibs, R. Wheeler and A. Ng, "ROS: an open-source Robot Operating System," *ICRA Workshop on Open Source Software*, 1 2009.